nature catalysis

Article

https://doi.org/10.1038/s41929-024-01181-w

Localized thermal levering events drive spontaneous kinetic oscillations during CO oxidation on Rh/Al_2O_3

Received: 19 August 2022

Accepted: 28 May 2024

Published online: 2 July 2024

Check for updates

Donato Decarolis[1,2,3], Monik Panchal[2,4,5], Matthew Quesne[1,2], Khaled Mohammed[6,7], Shaojun Xu[1,2,8], Mark Isaacs[4,9], Adam H. Clark[10], Luke L. Keenan[3], Takuo Wakisaka[11], Kohei Kusada[11,12], Hiroshi Kitagawa[11], C. Richard A. Catlow[1,2,4], Emma K. Gibson[2,13], Alexandre Goguet[2,14] ✉ & Peter P. Wells[2,3,6] ✉

Unravelling kinetic oscillations, which arise spontaneously during catalysis, has been a challenge for decades but is important not only to understand these complex phenomena but also to achieve increased activity. Here we show, through temporally and spatially resolved operando analysis, that CO oxidation over Rh/Al_2O_3 involves a series of thermal levering events—CO oxidation, Boudouard reaction and carbon combustion—that drive oscillatory CO_2 formation. This catalytic sequence relies on harnessing localized temperature episodes at the nanoparticle level as an efficient means to drive reactions in situations in which the macroscopic conditions are unfavourable for catalysis. This insight provides a new basis for coupling thermal events at the nanoscale for efficient harvesting of energy and enhanced catalyst technologies.

Understanding the spontaneous oscillatory behaviour of catalytic performance has provided an ongoing challenge since this was first reported in the 1970s[1–4]; the phenomenon is characterized by notable swings in activity that periodically alternate between high and low output. We need to determine the events that drive these variations in productivity and, if possible, use this knowledge as a basis for harnessing the improved kinetics at the maxima of catalytic turnover. Such behaviour has been observed with many oxidation reactions (for example, of propane and methane)[5–13]. CO oxidation is one of the reactions in which this phenomenon appears and has been used as a model reaction to understand the mechanism behind this behaviour. In the case of platinum, palladium and rhodium, extensive studies have been performed on model systems under idealized conditions (for example, single crystals and ultrahigh vacuum)[14–19]. For both platinum and palladium, these oscillations have been ascribed to reversible surface phase transitions. Vendelbo et al. were able to visualize these changes using high-resolution in situ transmission electron microscopy[20]. However, when considering more realistic conditions, other parameters have to be taken in account, such as oxide formation and in-plane restructuring.

In this regard, X-ray spectroscopy has been an important tool in identifying the key information regarding the oxidation state and the

[1]Cardiff Catalysis Institute, School of Chemistry, Cardiff University, Cardiff, UK. [2]UK Catalysis Hub, Research Complex at Harwell, Rutherford Appleton Laboratory, Harwell, UK. [3]Diamond Light Source, Harwell Science and Innovation Campus, Didcot, UK. [4]Department of Chemistry, University College London, London, UK. [5]Department of Chemistry, Durham University, Durham, UK. [6]School of Chemistry, University of Southampton, Southampton, UK. [7]Chemistry Department, Faculty of Science, Sohag University, Sohag, Egypt. [8]Department of Chemical Engineering, University of Manchester, Manchester, UK. [9]Harwell XPS, Research Complex at Harwell, Rutherford Appleton Laboratory, Didcot, UK. [10]Paul Scherrer Institute, Villigen, Switzerland. [11]Division of Chemistry, Graduate School of Science, Kyoto University, Kyoto, Japan. [12]The Hakubi Center for Advanced Research, Kyoto University, Kyoto, Japan. [13]School of Chemistry, Joseph Black Building, University of Glasgow, Glasgow, UK. [14]Queen's University Belfast, School of Chemistry and Chemical Engineering, Belfast, UK. ✉e-mail: a.goguet@qub.ac.uk; p.p.wells@soton.ac.uk

local geometry of the nanoparticles involved. Using this approach, it has been discovered that this phenomenon originates from the bistability[14–18] of different phases (metallic and oxidic) under analogous conditions, or as a consequence of the changing local environment (for example, temperature, gas composition) that takes place at the point of catalytic light-off. For both the palladium and platinum cases, operando analysis has been able to follow the changes in metal speciation during the periodic fluctuation in CO_2 production[19–24]. In the case of platinum, it has been shown by Singh et al. that this oscillatory behaviour is due to the absorption of CO on the platinum nanoparticles, which lowers the activity[25]. Subsequently, local fluctuations in CO concentration cause the CO-covered platinum surface to react with the surface oxide, causing a sudden ignition, during which CO disappears from the surface and platinum is oxidized[25]. Dann et al. have shown a similar behaviour happening on Pd/Al_2O_3, where the rate-limiting step is the dissociative absorption of O_2 on the nanoparticles, and CO acts as a poison, reducing the reaction rate to the low-activity regime[24].

However, in the case of supported rhodium catalysts, despite exhaustive studies, there has been no report of spectroscopic signatures that vary in phase with the catalytic activity[19,26–28]. The periodic behaviour of signals in previous operando studies is limited to mass spectrometry data and spikes in gas-phase CO_2 from the headspace of an operando sample environment, and is postulated to derive from the burn-off of adsorbed carbonaceous material[27]. The precise series of events, supported through spectroscopic analysis, has remained elusive. Furthermore, Dann et al. and Singh et al. demonstrated a dramatic dependence of the catalyst nature on the spatial position across a packed-bed reactor[24,25]. In particular, Dann et al. were able to follow the kinetic oscillations of CO oxidation over Pd/Al_2O_3 and found that only the inlet of the reactor influenced the end-pipe mass spectrometry (MS) oscillations[24]. This need for spatial analysis during spectroscopic investigations is often overlooked, that is, determining which points of a catalytic fixed-bed reactor truly contribute to the oscillatory behaviour[29–32]. This can provide crucial information that is often missing in the commonly used single-point analysis.

We have now performed a temporally and spatially resolved study of $Rh/\gamma\text{-}Al_2O_3$ that combines X-ray absorption spectroscopy, diffuse reflectance infrared Fourier transform spectroscopy (DRIFTS) and end-pipe MS, and observed oscillatory behaviour in each of the analytical methods. This study identifies a series of localized thermal levering events that are the source of the oscillatory behaviour of rhodium-catalysed CO oxidation: the localized heat generated by CO oxidation is sufficient to promote the Boudouard reaction ($2CO \rightarrow C + CO_2$)[33–35] and the oscillations are the result of successive burn-off cycles of accumulated carbon.

Results

Operando X-ray absorption fine structure/DRIFTS investigations

A sample of 4 wt% $Rh/\gamma\text{-}Al_2O_3$ was prepared through a wetness impregnation method which yielded well-dispersed rhodium particles with an average size of 1.9 nm as confirmed by high-angle annular dark-field scanning transmission electron microscopy (Supplementary Fig. 1). This was further supported by extended X-ray absorption fine structure (EXAFS) analysis of the reduced form of the catalyst (Supplementary Fig. 8)[36]. We then performed a spatially resolved, combined DRIFTS/EDE (energy-dispersive EXAFS) investigation, in conjunction with end-pipe MS analysis, using our recently reported, custom-designed operando reactor (Supplementary Fig. 3)[24]. This study assessed different axial positions during a controlled temperature ramp under CO oxidation conditions. At each position the catalyst was regenerated to the initial state by a series of reduction–oxidation–reduction cycles at elevated temperatures, generating a reproducible initial X-ray absorption near-edge structure (XANES) spectrum (Supplementary Fig. 8)[27]. To achieve reliable EDE data, it was crucial to avoid photon-induced beam damage[37–39], for example, by reducing the beam flux to ~10% of the maximum (Supplementary Figs. 4–15). By assessing the normalized intensity of the initial XANES peak at 23,238 eV, we were able to track the progression of the reaction front, that is, as the reaction proceeds the catalyst becomes progressively oxidized (Fig. 1). This initiated at the outlet of the catalyst bed and propagated towards the inlet, consistent with other spatially resolved studies[24,29,30]. Interestingly, we were able to observe oscillatory behaviour in the end-pipe MS analysis, the intensity of adsorbed carbonyl bands through DRIFTS and the intensity of the XANES white line at each spatial position (Supplementary Figs. 17–21)[27]. We have used the outlet of the reactor (axial position 6) to illustrate the series of linked events (Fig. 2). Furthermore, we performed EXAFS analysis at different axial positions to ensure there was no observable particle growth, either as a function of position or successive regeneration cycles (Supplementary Fig. 35 and Supplementary Table 4).

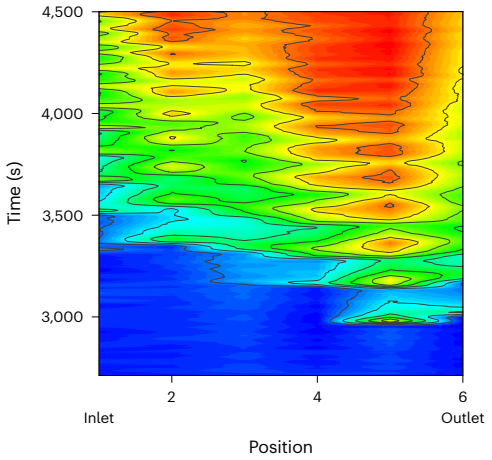

Fig. 1 | Evolution of Rh K edge XANES. White-line intensity at 23,238 eV during CO oxidation on Rh/Al_2O_3 as a function of time and position along the catalyst bed. The colour indicates the intensity of the white line at each spatial position (red highest, blue lowest) during the temperature ramp. Reaction conditions: 1% CO, 3% O_2, He to balance; temperature ramp, 91–139 °C (2 °C min^{-1}).

The end-pipe MS data show the calibrated m/z responses for CO_2, CO and O_2. In the period between 0 and ~2,800 s we observed no change to the mass spectrometry, while plotting the intensity of the two $Rh^1(CO)_2$ bands as a function of time shows a steady increase in the intensity of these two bands. This change, however, cannot be ascribed to a change in structure of the rhodium nanoparticles, as confirmed by multivariate curve resolution (MCR) analysis of the XANES (Supplementary Fig. 39), as well as the EXAFS Fourier transform analysis (Supplementary Fig. 40). As time, and by extension the external temperature, increased we observed a gradual decrease in the levels of CO and O_2, with a concomitant rise in the level of CO_2. These steady changes are punctuated by periodic events, during which sharp bursts of CO_2 production and CO and O_2 consumption are observed. This behaviour is different from that observed for Pd/Al_2O_3, in which the bursts of CO_2 were not correlated to a decrease in the concentration of CO. In the case of palladium, the increased CO_2 production was rationalized by the removal of sequestered CO adsorbed on the catalyst surface, that is, the CO_2 production did not require additional gas-phase CO. In this study on Rh/Al_2O_3, when we compared the end-pipe MS data to portions of the XANES (white-line intensity at 23,238 eV) (see Supplementary Fig. 37 for the full MCR analysis) and DRIFTS (adsorbed carbonyl, 2,060 cm^{-1} (linear) and 1,889 cm^{-1} (bridging), gas-phase CO_2, 2,340 cm^{-1}) spectra (see Supplementary Figs. 33 and 34 for full infrared spectra)[40], distinct oscillatory behaviour was also observed. During the spikes of CO_2 production, the XANES data indicated increased oxidation of rhodium at the CO_2 peak maxima; the reaction was carried out in an excess of O_2 and as more CO is consumed at these points a more oxidized form

https://doi.org/10.1038/s41929-024-01181-w

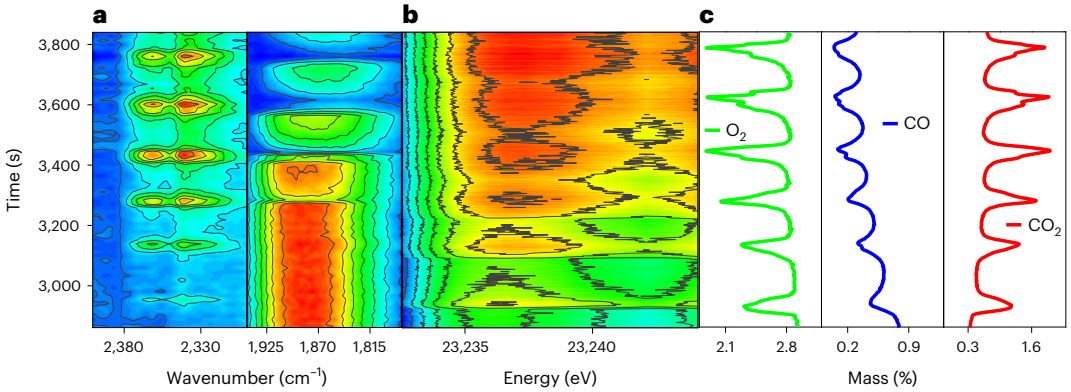

Fig. 2 | Combined XAFS, DRIFTS and MS analysis. a, Evolution of DRIFTS signature in the regions that correspond to adsorbed CO_2, from 2,400 to 2,300 cm^{-1} (left) and CO, from 1,945 to 1,781 cm^{-1} (right) (red highest, blue lowest). **b**, Evolution of Rh K edge XANES from 23,233 to 23,244 eV (red highest, blue lowest). **c**, Evolution of CO_2, CO and O_2 concentration derived from MS (m/z = 44, 28 and 32, respectively) as a function of time at the catalyst bed outlet during the temperature ramp (axial position 6). Reaction conditions: 1% CO, 3% O_2, He to balance; temperature ramp, 91–123 °C (2 °C min^{-1}).

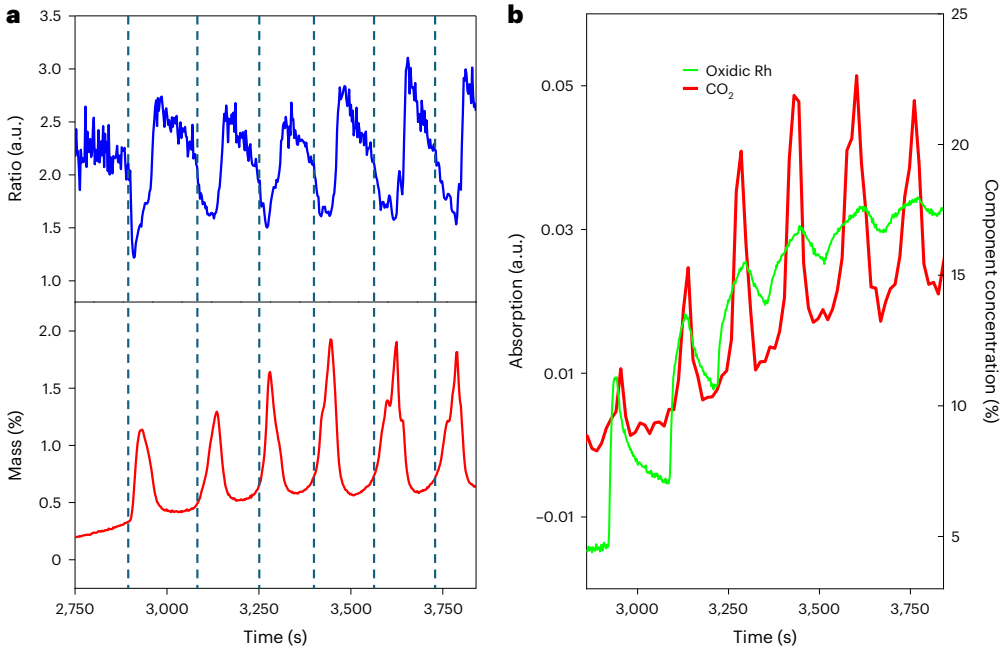

Fig. 3 | Assessing the product/reactant ratio and its impact on catalyst speciation with increasing temperature. a, Ratio between instantaneous CO_2 produced and O_2 consumed (top) and CO_2 produced (bottom) obtained from MS. The grey dashed lines indicate the region in which the CO_2 spike appears due to carbon combustion. **b**, Baseline-corrected DRIFTS intensity of the peak at 2,336 cm^{-1} for CO_2(g), plotted versus rhodium-defective oxide percentage, obtained from MCR analysis of XANES, as a function of time for axial position 6 during the CO oxidation temperature ramp. Reaction conditions: 1% CO, 3% O_2, He to balance; temperature ramp, 91–121 °C (2 °C min^{-1}).

of the catalyst is expected, consistent with other operando studies in this area[24].

With respect to the DRIFTS, we observe fluctuation in the infrared bands associated with gas-phase CO_2 and adsorbed carbonyl species, with the same periodicity as the features associated with the XANES and MS data. Considering that the spectroscopic signatures originated from discrete axial positions, and the MS data represented the summation of the entirety of the catalyst bed, it is curious that the phasing of different forms of analysis were synchronized in this way. Indeed, when we assessed the XANES data, as a function of position (Fig. 1), we observed that these oscillations were always in phase with the end-pipe MS data, regardless of position and do not appear to be due to a change of particle size as evidenced by the EXAFS (Supplementary Fig. 38 and Supplementary Tables 4 and 5). This suggested that there was a 'trigger' that initiated the series of events throughout the catalyst bed.

To investigate this in more detail, we assessed the relative fractions of CO and O_2 during the experiments (Fig. 3). We also analysed the adsorbed carbonyl bands identified through our DRIFTS data (Supplementary Fig. 27): $Rh^1(CO)_2$, 2,092 cm^{-1} (symmetric) and 2,020 cm^{-1} (asymmetric), and Rh(CO) associated with rhodium oxidation >1 at 2,132 cm^{-1}. Plotting the intensity of the two $Rh^1(CO)_2$ bands as a function of time shows that the intensity increases steadily until 'light off', when it stops increasing and plateaus. When comparing the normalized data for the $Rh^1(CO)_2$, $Rh^0{}_2(CO)$ and $Rh^0(CO)$ species it is possible to see that the $Rh^1(CO)_2$ species are not subject to the same oscillatory process that occurs on the Rh^0, suggesting a lack of involvement in the oxidative process. This is not the case for $Rh^{>1}(CO)$ species, where it is possible to see a behaviour akin to the oscillatory features exhibited by the $Rh^0(CO)$ species, albeit with some difference. In particular, it appears that during a 'spike' in CO_2 production, as the concentration

https://doi.org/10.1038/s41929-024-01181-w

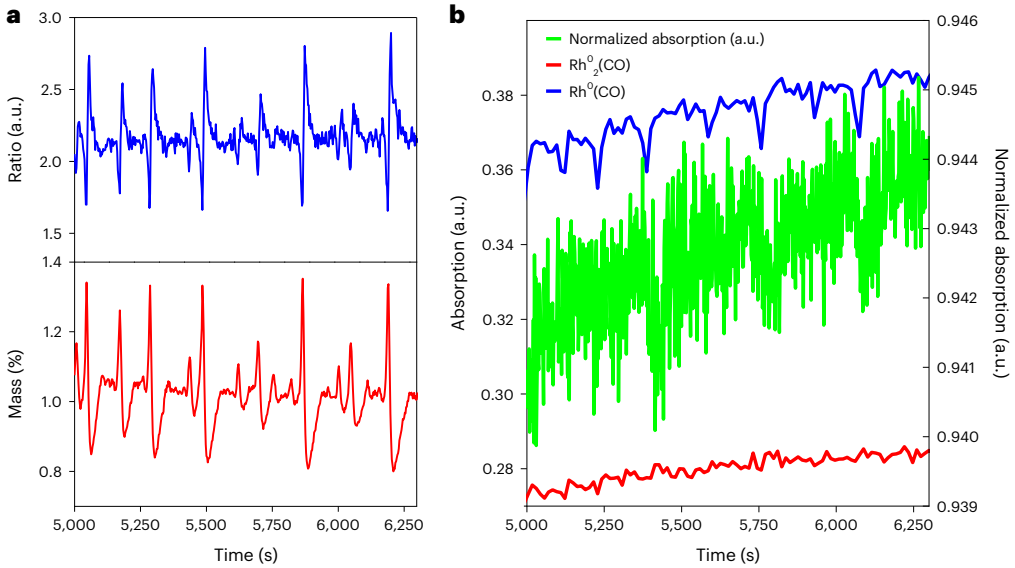

Fig. 4 | Assessing the product/reactant ratio and its impact on catalyst speciation during the isothermal window. a, CO_2 produced:O_2 consumed ratio and CO_2 produced obtained from MS. **b**, Baseline-corrected DRIFTS intensity of the peaks at 2,336 cm^{-1} (CO_2(g)) and 2,060 cm^{-1} (Rh^0_2(CO)) plotted with normalized XANES white line, at 23,238 eV, trace, as a function of time for the axial position 6 during CO oxidation at isothermal at 150 °C. Reaction conditions: 1% CO, 3% O_2, He to balance.

of Rh^0(CO) drops, the $Rh^{>1}$(CO) species signal increases, simultaneously with the observed increase in oxidic fraction derived from MCR analysis of the XANES results (Fig. 3; see Supplementary Fig. 37 for the full MCR analysis). However, the lack of a decrease in the amount of $Rh^{>1}$(CO) species upon catalyst reduction suggests that these species are not involved in the reaction process, and they increase only due to the steady increase in the oxidation state of rhodium.

Assessing the ratio between CO_2 produced and O_2 consumed allowed us to investigate parallel reactions. For CO oxidation, whether the CO_2 derives from adsorbed/sequestered CO or from gas-phase CO, the CO_2 produced/O_2 consumed ratio is equal to 2 based on the reaction stoichiometry. However, the ratio observed fluctuated between ~1.2 and 3, with the same periodicity as observed for the bursts of CO_2 production. This indicated that additional reactions were involved. Considering our reactants (CO_2 and O_2), the only plausible process that can generate CO_2, and require less O_2 than direct CO oxidation (equation (1)), is the Boudouard reaction, which produces CO_2 without consuming any oxygen. A combination of CO oxidation and Boudouard reaction (equation (2)) would result in a CO_2 produced/O_2 consumed ratio >2 and is also consistent with the reaction stoichiometry prior to 'light-off'. The other associated product of the Boudouard reaction is carbon. When we assessed the points of maximum CO_2 production, the ratio of CO_2 produced/O_2 consumed dropped to a minimum value (<2). This indicated that more O_2 was being consumed to produce CO_2 than is required by direct CO oxidation and is consistent with the combustion of carbon to produce CO_2 (equation (3)).

$$2CO + O_2 \rightarrow 2CO_2 \quad CO_2 \text{ produced} : O_2 \text{ consumed} = 2 \qquad (1)$$

$$2CO \rightarrow CO_2 + C \quad CO_2 \text{ produced} : O_2 \text{ consumed} = \infty \qquad (2)$$

$$C + O_2 \rightarrow CO_2 \quad CO_2 \text{ produced} : O_2 \text{ consumed} = 1 \qquad (3)$$

The observed CO_2 produced/O_2 consumed ratio of between 1 and 2 is consistent with a mixture of carbon combustion and direct CO oxidation. Coupling these events together, we propose: (1) that prior to 'light off' there is a mixture of CO oxidation and the Boudouard reaction that deposits carbon, (2) at a certain point the combustion of carbon is initiated, which triggers an associated exotherm (which travels throughout the catalyst bed as seen in Fig. 1) and burns off any laid-down carbon, and (3) this process then repeats itself. An alternative mechanism could involve abstracting oxygen from rhodium oxide clusters to produce CO_2 without consuming any oxygen. However, this would require consumption of the surface oxygen and would be associated with a concomitant decrease in rhodium oxide. When we assessed the CO band associated with $Rh^{>1}$ (Supplementary Fig. 27), we observed that rather than decreasing the band remained constant during these temporal regions. regions. Moreover, Gustafsson and co-workers have established metallic rhodium to be the active surface for this reaction[41]. This allowed us to discount this alternative series of events. Our initial hypothesis is further confirmed by the speciation of carbon using X-ray photoelectron spectroscopy (Supplementary Figs. 28 and 29) which shows a >2-fold increase in the amount of CC/CH species with a spent catalyst compared with its fresh state. As no carbon species other than CO in the feed are present, this increase can only be explained by a deposition of carbon, be it amorphous or graphitic, on the surface of the catalyst as a consequence of the Boudouard reaction. More importantly, a sudden drop in performance is not consistent with solely CO oxidation; the reaction is heavily exothermic and one would anticipate a conventional light-off behaviour. Indeed, the linked behaviour of these thermally levered reactions should manifest themselves by a reduction of oscillatory behaviour when the catalyst is diluted. We observed that the intensity of the oscillations was negligible compared to the pure catalyst when diluting the catalyst in SiC (dilutions of 1:10 and 1:20 Rh/Al_2O_3:SiC; Supplementary Figs. 41 and 42).

We assessed the possibility of rhodium carbide formation[34], as previously suggested during CO oxidation on rhodium, by comparing the structure of a recently reported Rh_2C (ref. 42) with the XANES results (Supplementary Fig. 30). However, the data could not support the formation of this species. Prins and Koningsberger assessed Rh/γ-Al_2O_3 catalysts during the Boudouard reaction and proposed that aspects of the EXAFS data could be consistent with the presence of a rhodium-carbide-like structure[34]. However, the authors also report notable complexity with the EXAFS data and that exact confirmation on the nature of rhodium species was hard to extract. Elsewhere within catalysis research, there are an increasing number of papers that report the presence of carbide structures that form during catalysis

https://doi.org/10.1038/s41929-024-01181-w

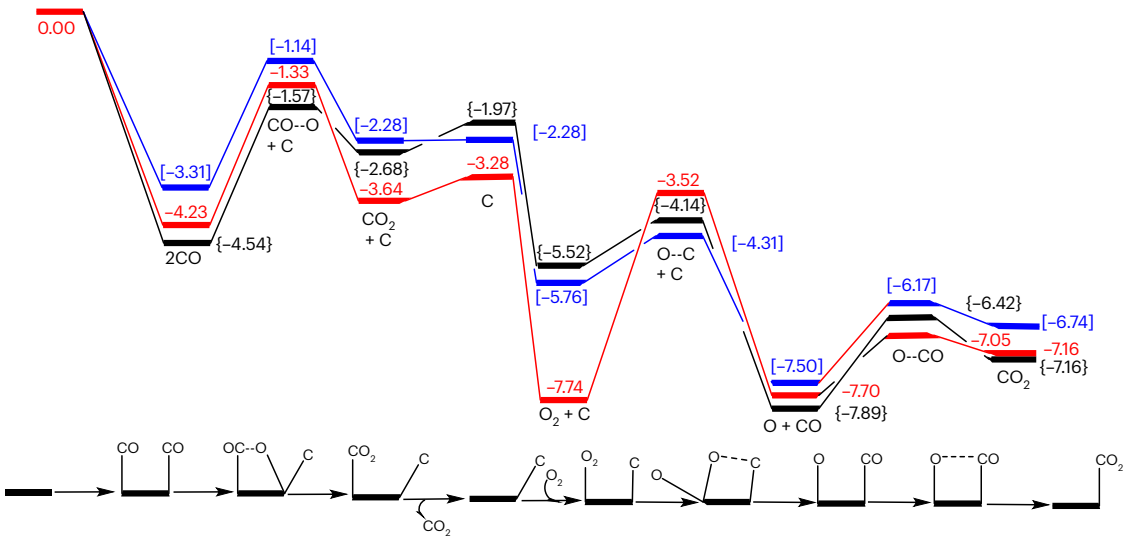

Fig. 5 | Potential energy landscape for the coupled Boudouard and carbon combustion reactions. Values are recorded for the 001 (red line), {011} (blue line) and [111] (black line) surfaces and a schematic representation of the surface steps is depicted. All energies were obtain using UPBE and given in eV, relative to the pristine surfaces that acts as both a starting and end point for the complete catalytic cycle.

(for example, for palladium on exposure to acetylene, ethene[43], and during furfural hydrogenation[44]). Considering the growing awareness of the role of carbides in catalysis and that the Boudouard reaction generates elemental carbon, we decided to explore this in more detail. Recently, methods have been established for the facile synthesis of transition-metal carbides including Rh_2C (ref. 42). Using the Rh_2C from this published work we acquired XAFS data to compare to our data collected under reaction conditions (Supplementary Fig. 30). Using both a visual comparison and multivariate curve resolution approaches we could not identify or abstract any carbide-like components from the XANES data; indeed, there are major differences between the XANES of the Rh_2C spectra and that acquired during our time-resolved studies. Based on these observations, there was nothing within this study to suggest that rhodium carbide was formed during catalysis or was responsible for any of the oscillatory behaviour.

At the end of the temperature ramp, we continued to collect data under isothermal conditions (Fig. 4). Interestingly, we still observed periodic fluctuations in the CO_2 production (and associated CO_2 produced/O_2 consumed ratio). However, the lifetime of these events was markedly reduced and now appeared as sharper spikes in the data. Throughout the broad oscillations found during the temperature ramp, we identified periodic fluctuations in the intensity of adsorbed carbonyl (both bridged and linear) bands and the XANES features associated with oxidic/metallic rhodium. Interestingly, under isothermal conditions, the MS-recorded spikes observed in the CO_2 concentration only manifested themselves in the data for rhodium adsorbed linear carbonyl, that is, the bridge-bonded carbonyl did not display any signal periodicity. We propose that this observation may be indicative of a site specificity for the deposition—and subsequent combustion—of the carbon associated with the Boudouard reaction

DFT calculations

To further explore the contribution of the Boudouard reaction, we assessed the reaction of CO over our Rh/Al_2O_3 catalyst in the absence of oxygen. We found that the Boudouard reaction was initiated at a temperature of 600 °C (Supplementary Fig. 31). If higher macroscopic temperatures are required to promote the Boudouard reaction over this catalyst, what promoted the reaction during our CO oxidation study? Our work on non-thermal plasma-assisted catalysis has previously established that the temperatures experienced, at the level of the particle, can be in excess of the macroscopic temperature—for example, an exothermic reaction generates localized heat at a NP surface that is subsequently dissipated to the macroscopic environment[45]. In this study, we propose that the exothermicity of CO oxidation is sufficient to drive the Boudouard reaction at lower macroscopic temperatures. To evaluate this result, we performed a series of DFT calculations (using periodic boundary conditions techniques implemented in the VASP code[46–48]) of the reaction path of both direct CO oxidation and alternating pathways of the Boudouard reaction (Supplementary Fig. 32). All energies reported here refer to values obtained in combination with the Perdew–Burke–Ernzerhof[49] exchange functional, although major trends were replicated with the metaGGA (SCAN) functional[50]. The ambient-phase face-centred cubic structure of rhodium was fully optimized[51] before this structure could be cut along its low-index planes using the METADISE code[52,53]. Each slab was constructed by doubling the primitive cell in each Cartesian direction to produce slabs with four atomic layers in the *z* direction. Reactivity appeared to be greatest on the (011) and (111) surfaces with carbon oxidation to CO proceeding with a barrier of <1.5 eV. For comparison, the rate-limiting barriers for the Boudouard reaction mechanism was judged to be consistently >2.5 eV, which would be inaccessible under reaction conditions of less than 600 K. Using standard thermodynamic tables[54] it is established that the maximum total localized energy contribution from CO oxidation is approximately −2.9 eV at 300 K. The liberated reaction energy from CO oxidation is more than sufficient to overcome the high Boudouard barrier and is an agreement with our postulated series of events. The full reaction landscapes of the alternating Boudouard reaction and carbon combustion was subsequently constructed from these energies (Fig. 5), with these results confirming the very exothermic nature of these processes.

Discussion

Spontaneous kinetic oscillations during heterogeneous catalysis have garnered considerable attention over several decades[20,24,55]. Model studies on palladium[24] and platinum[25] catalysts for CO oxidation have identified the role of structural bistability, where the catalyst fluctuates between different active states. In this study, we propose that thermal levering of connected reactions drives this behaviour. Specifically, through both experimental and theoretical studies we confirm that exothermic CO oxidation facilitates the Boudouard reaction, which lays down elemental carbon that is periodically exhausted to create the oscillations in CO_2 output. Our spatially resolved combined DRIFTS/EDE

spectroscopic study was able to identify changes in rhodium speciation throughout the oscillatory phenomena. These investigations both confirm that the fractions of Rh^0 and $Rh^{>1+}$ fluctuate throughout the oscillatory behaviour, with rhodium becoming progressively oxidized throughout the temperature profile. The inherent kinetic performance of these phases towards CO oxidation cannot explain the end-pipe MS data. The alterations in outlet composition confirm that multiple reactions are taking place; to achieve a CO_2 produced:O_2 consumed ratio >2 requires a different process to CO oxidation, regardless of whether the CO is adsorbed on the catalyst surface or from the gas phase. Considering the reactants, the only plausible explanation is a combination of CO oxidation and the Boudouard reaction. More importantly, a sudden drop in performance is not consistent with solely CO oxidation; the reaction is heavily exothermic and one would anticipate a conventional light-off behaviour.

Moreover, we see at higher macroscopic temperatures and lower CO coverage that the reaction still proceeds. These observations point to an exhaustible supply of carbon that is responsible for the bursts in CO_2 production, which were subsequently confirmed by ex situ XPS analysis. This is also consistent with previous operando analysis that suggested deposited carbon was responsible for spikes in CO_2 production in the headspace of a conventional DRIFTS set-up.

These results are also consistent with emerging work elsewhere within the field of heterogeneous catalysis. Our work on non-thermal plasma-assisted catalysis has demonstrated that the temperature achieved at the level of the nanoparticle can greatly exceed what is measured macroscopically[45]. Elsewhere, combining autothermal processes within the same sites is developing into an emerging area. Recent work has demonstrated how ammonia decomposition (endothermic) can be combined with small amounts of selective ammonia oxidation (exothermic) to facilitate the process without any external temperature stimulus[56]. These approaches offer unique ways to develop the catalytic processes that are required for future technologies.

Methods

Sample preparation

Synthesis of Rh/γ-Al_2O_3 was performed according to a method similar to that described by Kroner et al.[57] γ-Al_2O_3 (4.80 g, 47 mmol) was suspended in water (150 ml) and stirred at 350 rpm for 5 min. To the resulting cloudy white solution, $RhCl_3{\cdot}xH_2O$ (0.535 g, 2.56 mmol) was added as it was stirred, which resulted in a cloudy red solution which was left to stir for 30 min. Sample was filtered and left to dry overnight in air, to afford a light red solid (4.80 g) which was calcined under 20% O_2/He for 6 h at 400 °C then reduced under pure H_2 at 300 °C for 5 h which formed a black solid of Rh/γ-Al_2O_3.

Combined operando EDE/DRIFTS/MS measurements

In situ XAFS measurements were obtained at I20-EDE, the energy-dispersive beamline of the Diamond Light Source (UK). Dispersive XAFS at the Rh K-edge (24,358 eV) were collected in transmission mode using a Si(3 1 1) polychromator and a FReLoN charge-coupled device camera as the X-ray detector. The dispersive X-ray beam was focssed at the sample to a spot size of 0.5 mm horizontally and 0.15 mm vertically.

The wiggler was opened from 18.5 mm (1.3 T) to 27 mm (0.86 T) which reduced the incident flux by two-thirds (to 34.66% of the maximum flux possible). We then used 25 µm molybdenum, 10 µm lead and 4.8 mm carbon filters. These attenuators reduce the beam to 9.7% of the incident flux, that is, a factor of 10 reduction. The reaction cell used for synchronous, spatially resolved EDE and DRIFTS measurements was designed at the UK Catalysis Hub. The reaction cell was constructed from pure grade aluminium with a square cross-sectional channel, measuring 5 mm × 5 mm, to contain the catalyst sample. The aluminium walls on two sides of the reactor were thinned to 250 µm by drilling a 50 mm length trench along the sample channel for transmission of X-rays through the cell and sample. A rectangular 52 mm × 7 mm CaF_2 window was fitted to the top face of the reactor for infrared transmission to and from the catalyst surface. Gas lines were fitted to both ends of the cell with Swagelok fittings and a K-type Inconel thermocouple was inserted through one end of the reactor to measure the temperature of the catalyst sample. The tip of the thermocouple was positioned at the end of the reactor nearest the reactor outlet and so measured the local temperature at the end position of the catalyst bed. A heating plate was positioned beneath the reactor, and controlled by an external thermocouple. An Agilent Carey 680 FTIR spectrometer was positioned in the experimental hutch and used a DaVinci arm accessory fitted with praying mantis optics to refocus the infrared beam to the catalyst surface within the DRIFTS/EDE cell. MS data of the reactor exhaust were collected using an EcoCat mass spectrometer. First, 400 mg of the 4% Rh/γ-Al_2O_3 catalyst and 200 mg of bare γ-Al2O3 were sieved to a pellet fraction of 250–355 µm and loaded separately into the reactor so that the γ-Al_2O_3 sat upstream of the catalyst, and was held in place by quartz wool. The bare γ-Al_2O_3 was used as a reference to account for the absorption and scattering of the polychromatic X-ray beam by the support material, and as the background for DRIFTS spectra. The Rh/γ-Al_2O_3 catalyst bed extended a length of 18 mm and DRIFTS/EDE measurements were collected at six different spatial positions along its length. The catalyst was pretreated with a sequence of 4%H_2/Ar, 20% O_2/Ar, 4% H_2/Ar at 150 °C, then cooled to room temperature in argon to reduce and clean the catalyst prior to each run. The reactant gas feed (1%CO/3%O_2/Ar) was introduced into the sample at a total flow rate of 50 ml min^{-1} and allowed to reach steady state before ramping the temperature at 2 °C min^{-1} to 150 °C, collecting EDE, DRIFTS and MS measurements continuously. Each EDE spectrum was acquired in 6.5 ms to collect information of the XANES region and used 200 accumulations for EXAFS analysis. DRIFTS spectra were collected with 32 accumulations per spectrum, giving a time resolution of 13.2 s per spectrum and using a background collected from the bare γ-Al_2O_3 surface, in the reactant (CO/O_2/Ar) gas feed. The MS signal was normalized relative to the argon signal ($m/z = 20$) to account for any detector variation. The CO signal ($m/z = 28$) was corrected for contributions from CO_2 fragmentation by subtracting 10% of the value of $m/z = 44$.

XAFS data analysis

XAFS data normalization was performed using DAWN software[58]. The XANES linear combination fit was performed on Athena software[59] using Rh^0 and Rh_2O_3 references. EXAFS was analysed using Artemis software[59,60]. The FEFF6 code was used to construct theoretical EXAFS signals that included single-scattering contributions from atomic shells through the nearest neighbours, using rhodium as scatterer. The fit was performed using a k range between 3 and 11.5 $Å^{-1}$ and an R range between 2.2 and 3 Å. The amplitude reduction factor (S_0^2) was fixed at 0.69, and the thermal disorder factor (σ^2) was fixed at 0.003 as obtained from fitting the bulk rhodium foil reference.

XPS data acquisition

XPS data were acquired using a Kratos Axis SUPRA with monochromated Al Kα (1,486.69 eV) X-rays at 15 mA emission and 12 kV (180 W) and a spot size/analysis area of 700 × 300 µm. The instrument was calibrated to gold metal Au 4f (83.95 eV) and dispersion adjusted to give a binding energy of 932.6 eV for the Cu $2p_{3/2}$ line of metallic copper. The Ag $3d_{5/2}$ line full width at half maximum at 10 eV pass energy was 0.544 eV. The source resolution for monochromatic Al Kα X-rays is ~0.3 eV. The instrument resolution was determined to be 0.29 eV at 10 eV pass energy using the Fermi edge of the valence band for metallic silver. Resolution with the charge compensation system implemented was <1.33 eV full width at half maximum on polytetrafluoroethylene. High-resolution spectra were obtained using a pass energy of 20 eV, a step size of 0.1 eV and a sweep time of 60 s, resulting in a line width of 0.696 eV for Au $4f_{7/2}$. Survey spectra were obtained using a pass energy of 160 eV. Charge neutralization was achieved using an electron flood

gun with filament current of 0.38 A, a charge balance of 2 V and a filament bias of 4.2 V. Successful neutralization was judged by analysing the C 1*s* region wherein a sharp peak with no lower binding energy structure was obtained. Spectra were charge corrected to the main line of the C 1*s* spectrum set to 284.8 eV. All data were recorded at a base pressure of $<9 \times 10^{-9}$ torr and a room temperature of 294 K. Data were analysed using CasaXPS v.2.3.19PR1.0. Peaks were fit with a Shirley background prior to component analysis. Peaks were fit using an LA(1.53,243) lineshape. Air-free sample transfer to the Kratos XPS spectrometer was achieved as follows: the reaction was performed ex situ using the same experimental conditions as utilized during the operando experiment. The reactor was sealed using Swagelok gas taps and transported to the Kratos front loading glovebox, which had previously been filled with N_2.

Computational calculations

All calculations were performed with the Vienna Ab initio Simulation package[46–48], which was used to test several types of generalized gradient approximation functionals within the framework of periodic density functional theory. Results obtained using the standard version of the Perdew–Burke–Ernzerhof[50] exchange functional were supplemented by the metaGGA (SCAN)[49]. Plane-wave basis sets were applied to the valence electrons, whereas the core electrons were described by the projected augmented wave method developed by Blöchl[61]. Additionally, long-range interactions were modelled using the Grimme dispersion D3 method[62,63]. Monkhorst–Pack grids were used to add K points of $5 \times 5 \times 5$ to the bulk calculations and meshes of $5 \times 5 \times 1$ for the surface calculations. All energies converged within a cut-off of 520 eV, although different cut-off values and numbers of K points were also tested (Supplementary Information). The threshold for the ionic relaxation was set at 0.01 eV Å^{-1}. The electronic threshold for the self-consistency cycles was set to 10^{-5} eV.

Once all the different surfaces were fully relaxed, it was possible to assess surface energies (σ) and work functions (Φ). Surface energies for the unrelaxed surfaces (σ^u) were calculated using equation (4). A denotes the area of each surface with E_{slab} indicating the total energy of the unrelaxed slab and n standing for the number of bulk unit cells used to form the slab volume. The factor of 2 in the denominators is necessary because two surfaces are formed for each system.

$$\sigma^u = \frac{E_{slab} - nE_{bulk}}{2A} \quad (4)$$

$$\sigma^r = \frac{E_{relax} - nE_{bulk}}{A} - \sigma^u \quad (5)$$

When only half the slab is relaxed, the relaxed surface energy (σ^r) must be determined as shown in equation (5); here the area of only one surface is included in the denominator and this energy is subtracted from that of the unrelaxed surfaces.

Data availability

The data that support the findings of this study are available from the University of Southampton repository with the identifier https://doi.org/10.5258/SOTON/D3028.

References

1. Yang, C. H. & Berlad, A. L. Kinetics and kinetic oscillation in carbon monoxide oxidation. *J. Chem. Soc. Faraday Trans.* **70**, 1661–1675 (1974).
2. Dauchot, J. P. & Cakenberghe van, J. Oscillations during catalytic oxidation of carbon monoxide on platinum. *Nat. Phys. Sci.* **246**, 61–63 (1973).
3. Ertl, G., Norton, P. R. & Rüstig, J. Kinetic oscillations in the platinum-catalyzed oxidation of CO. *Phys. Rev. Lett.* **49**, 177–180 (1982).
4. Franck, K. R., Lintz, H.-G. & Tufan, G. Oscillatory instabilities in the oxidation of carbon monoxide on rhodium. *J. Catal.* **79**, 466–469 (1983).
5. Zhang, X., Lee, C. S.-M., Hayward, D. O. & Mingos, D. M. P. Oscillatory behaviour observed in the rate of oxidation of methane over metal catalysts. *Catal. Today* **105**, 283–294 (2005).
6. Zhang, X., Lee, C. S.-M., Mingos, D. M. P. & Hayward, D. O. Oscillatory behaviour during the oxidation of methane over palladium metal catalysts. *Appl Catal. A Gen.* **240**, 183–197 (2003).
7. Gladky, A. Y., Ermolaev, V. K. & Parmon, V. N. Oscillations during catalytic oxidation of propane over a nickel wire. *Catal. Lett.* **77**, 103–106 (2001).
8. Kaichev, V. V. et al. In situ XPS study of self-sustained oscillations in catalytic oxidation of propane over nickel. *Surf. Sci.* **609**, 113–118 (2013).
9. Okamoto, H., Tanaka, N. & Naito, M. Chaotic and periodic potential oscillations in formaldehyde oxidation. *J. Phys. Chem. A* **102**, 7343–7352 (1998).
10. Obuchi, A. et al. Self-oscillating behaviour in the selective catalytic reduction of NO by propene. *Chem. Commun.* https://doi.org/10.1039/C39920001150 (1992).
11. Kobayashi, M., Kanno, T., Takeda, H. & Fujisaki, S. Structure sensitivity of oscillating partial oxidation of propene on widely dispersed platinum catalysts. In *11th International Congress On Catalysis—40th Anniversary* vol. 101 (eds Hightower, J. W. et al.) 1059–1064 (Elsevier, 1996).
12. Schreyer, H., Immohr, S. & Schüth, F. Oscillatory combustion of propene during in situ mechanical activation of solid catalysts. *J. Mater. Sci.* **52**, 12021–12030 (2017).
13. Ochs, T. & Turek, T. The mechanism of kinetic oscillations in the catalytic N_2O decomposition over Cu-ZSM-5. *Chem. Eng. Sci.* **54**, 4513–4520 (1999).
14. Hendriksen, B. L. M., Bobaru, S. C. & Frenken, J. W. M. Bistability and oscillations in CO oxidation studied with scanning tunnelling microscopy inside a reactor. *Catal. Today* **105**, 234–243 (2005).
15. Hammoudeh, A. & Naschitzki, M. CO oxidation on palladium field emitter: kinetic oscillations and bistability. *Mater. Sci. Eng. A* **270**, 83–88 (1999).
16. Zhdanov, V. P. & Kasemo, B. The effect of oxide formation on bistability in CO oxidation on Pt. *J. Catal.* **220**, 478–485 (2003).
17. Kulginov, D., Zhdanov, V. P. & Kasemo, B. Oscillatory surface reaction kinetics due to coupling of bistability and diffusion limitations. *J. Chem. Phys.* **106**, 3117–3128 (1997).
18. Gorodetskii, V., Drachsel, W., Ehsasi, M. & Block, J. H. Field ion microscopic studies of the CO oxidation on platinum: bistability and oscillations. *J. Chem. Phys.* **100**, 6915–6922 (1994).
19. Ioannides, T., Efstathiou, A. M., Zhang, Z. L. & Verykios, X. E. CO oxidation over Rh dispersed on SiO_2, Al_2O_3 and TiO_2: kinetic study and oscillatory behavior. *J. Catal.* **156**, 265–272 (1995).
20. Vendelbo, S. B. et al. Visualization of oscillatory behaviour of Pt nanoparticles catalysing CO oxidation. *Nat. Mater.* **13**, 884–890 (2014).
21. Kaichev, V. V., Vinokurov, Z. S. & Saraev, A. A. Self-sustained oscillations in oxidation of methane over palladium: the nature of 'low-active' and 'highly active' states. *Catal. Sci. Technol.* https://doi.org/10.1039/D1CY00132A (2021).
22. Gänzler, A. M. et al. Operando spatially and time-resolved X-ray absorption spectroscopy and infrared thermography during oscillatory CO oxidation. *J. Catal.* **328**, 216–224 (2015).
23. Newton, M. A. Time resolved operando X-ray techniques in catalysis, a case study: CO oxidation by O_2 over Pt surfaces and alumina supported Pt catalysts. *Catalysts* https://doi.org/10.3390/catal7020058 (2017).

24. Dann, E. K. et al. Combined spatially resolved operando spectroscopy: new insights into kinetic oscillations of CO oxidation on Pd/γ-Al_2O_3. *J. Catal.* **373**, 201–208 (2019).
25. Singh, J., Nachtegaal, M., Alayon, E. M. C., Stötzel, J., & van Bokhoven, J. A. Dynamic structure changes of a heterogeneous catalyst within a reactor: oscillations in CO oxidation over a supported platinum catalyst. *ChemCatChem* **2**, 653–657 (2010).
26. Kroner, A. B. et al. Time-resolved, in situ DRIFTS/EDE/MS studies on alumina supported Rh catalysts: effects of ceriation on the Rh catalysts in the process of CO oxidation. *Catal. Struct. Reactivity* **3**, 13–23 (2017).
27. Figueroa, S. J. A. & Newton, M. A. What drives spontaneous oscillations during CO oxidation using O_2 over supported Rh/Al_2O_3 catalysts? *J. Catal.* **312**, 69–77 (2014).
28. Qin, F. & Wolf, E. E. Infrared thermography studies of unsteady-state processes during CO oxidation on supported catalysts. *Chem. Eng. Sci.* **49**, 4263–4267 (1994).
29. Stewart, C. et al. Unraveling the H_2 promotional effect on palladium-catalyzed CO oxidation using a combination of temporally and spatially resolved investigations. *ACS Catal.* **8**, 8255–8262 (2018).
30. Decarolis, D. et al. Spatial profiling of a Pd/Al_2O_3 catalyst during selective ammonia oxidation. *ACS Catal.* **11**, 2141–2149 (2021).
31. Schroer, C. G. & Grunwaldt, J.-D. in *In-situ Characterization of Heterogeneous Catalysts* (eds Rodriguez, J. A. et al.) 49–73 (Wiley, 2013); https://doi.org/10.1002/9781118355923.ch2
32. Touitou, J., Morgan, K., Burch, R., Hardacre, C. & Goguet, A. An in situ spatially resolved method to probe gas phase reactions through a fixed bed catalyst. *Catal. Sci. Technol.* **2**, 1811–1813 (2012).
33. Bost, N., Ammar, M. R., Bouchetou, M. L. & Poirier, J. The catalytic effect of iron oxides on the formation of nano-carbon by the Boudouard reaction in refractories. *J. Eur. Ceram. Soc.* **36**, 2133–2142 (2016).
34. Van't Blik, H. F. J., van Zon, J. B. A. D., Koningsberger, D. C. & Prins, R. EXAFS determination of the change in the structure of rhodium in highly dispersed Rh/γ-Al_2O_3 catalysts after CO and/or H_2 adsorption at different temperatures. *J. Mol. Catal.* **25**, 379–396 (1984).
35. Walker, P. L. Jr, Rakszawski, J. F. & Imperial, G. R. Carbon formation from carbon monoxide–hydrogen mixtures over iron catalysts. II. Rates of carbon formation. *J. Phys. Chem.* **63**, 140–149 (1959).
36. Beale, A. M. & Weckhuysen, B. M. EXAFS as a tool to interrogate the size and shape of mono and bimetallic catalyst nanoparticles. *Phys. Chem. Chem. Phys.* **12**, 5562–5574 (2010).
37. Albrahim, M. et al. Reduction and agglomeration of supported metal clusters induced by high-flux X-ray absorption spectroscopy measurements. *J. Phys. Chem. C* **125**, 11048–11057 (2021).
38. Bras, W., Newton, M. A., Myles, D. A. A. & Felici, R. High-intensity X-ray beams can influence the kinetics in a time-resolved experiment. *Nat. Rev. Methods Prim.* **2**, 22 (2022).
39. Jašík, J., Fortunelli, A. & Vajda, Š. Exploring the materials space in the smallest particle size range: from heterogeneous catalysis to electrocatalysis and photocatalysis. *Phys. Chem. Chem. Phys.* **24**, 12083–12115 (2022).
40. Cavers, M., Davidson, J. M., Harkness, I. R., Rees, L. V. C. & McDougall, G. S. Spectroscopic identification of the active site for CO oxidation on Rh/Al_2O_3 by concentration modulation in situ DRIFTS. *J. Catal.* **188**, 426–430 (1999).
41. Gustafson, J. et al. The role of oxides in catalytic CO oxidation over rhodium and palladium. *ACS Catal.* **8**, 4438–4445 (2018).
42. Wakisaka, T. et al. Rational synthesis for a noble metal carbide. *J. Am. Chem. Soc.* **142**, 1247–1253 (2020).
43. Jones, W. et al. Carbidisation of Pd nanoparticles by ethene decomposition with methane production. *ChemCatChem* **11**, 4334–4339 (2019).
44. Campisi, S. et al. Dual-site-mediated hydrogenation catalysis on Pd/NiO: selective biomass transformation and maintenance of catalytic activity at low Pd loading. *ACS Catal.* **10**, 5483–5492 (2020).
45. Gibson, E. K. et al. Probing the role of a non-thermal plasma (NTP) in the hybrid NTP catalytic oxidation of methane. *Angew. Chem. Int. Ed.* **56**, 9351–9355 (2017).
46. Kresse, G. & Furthmüller, J. Efficient iterative schemes for ab initio total-energy calculations using a plane-wave basis set. *Phys. Rev. B* **54**, 11169–11186 (1996).
47. Kresse, G. & Furthmüller, J. Efficiency of ab-initio total energy calculations for metals and semiconductors using a plane-wave basis set. *Comput. Mater. Sci.* **6**, 15–50 (1996).
48. Kresse, G. & Hafner, J. Ab initio molecular dynamics for liquid metals. *Phys. Rev. B* **47**, 558–561 (1993).
49. Perdew, J. P., Burke, K. & Ernzerhof, M. Generalized gradient approximation made simple. *Phys. Rev. Lett.* **77**, 3865–3868 (1996).
50. Bartók, A. P. & Yates, J. R. Regularized SCAN functional. *J. Chem. Phys.* **150**, 161101 (2019).
51. Moshopoulou, E. G., Ibberson, R. M., Sarrao, J. L., Thompson, J. D. & Fisk, Z. Structure of Ce_2RhIn_8: an example of complementary use of high-resolution neutron powder diffraction and reciprocal-space mapping to study complex materials. *Acta Crystallogr. B* **62**, 173–189 (2006).
52. Watson, G. W., Kelsey, E. T., de Leeuw, N. H., Harris, D. J. & Parker, S. C. Atomistic simulation of dislocations, surfaces and interfaces in MgO. *J. Chem. Soc. Faraday Trans.* **92**, 433–438 (1996).
53. Quesne, M., Roldan, A., Leeuw, N. & Catlow, R. Carbon dioxide and water co-adsorption on the low-index surfaces of TiC, VC, ZrC and NbC: a DFT study. *Phys. Chem. Chem. Phys.* **21**, 10750–10760 (2019).
54. Chase, M. *NIST-JANAF Thermochemical Tables*, 4th edn (American Institute of Physics, 1998).
55. Huang, Y. Y. Selective adsorption of carbon monoxide and complex formation of cuprous-ammines in Cu(I)Y zeolites. *J. Catal.* **30**, 187–194 (1973).
56. Nagaoka, K. et al. Carbon-free H_2 production from ammonia triggered at room temperature with an acidic RuO_2/γ-Al_2O_3 catalyst. *Sci. Adv.* **3**, e1602747 (2023).
57. Kroner, A. B. et al. Structural characterization of alumina-supported Rh catalysts: effects of ceriation and zirconiation by using metal–organic precursors. *ChemPhysChem* **14**, 3606–3617 (2013).
58. Basham, M. et al. Data Analysis WorkbeNch (DAWN). *J. Synchrotron Radiat.* **22**, 853–858 (2015).
59. Ravel, B. & Newville, M. Athena, Artemis, Hephaestus: data analysis for X-ray absorption spectroscopy using IFEFFIT. *J. Synchrotron Rad.* **12**, 537 (2005).
60. Newville, M. EXAFS analysis using FEFF and FEFFIT. *J. Synchrotron Radiat.* **8**, 96–100 (2001).
61. Blöchl, P. E. Projector augmented-wave method. *Phys. Rev. B* **50**, 17953–17979 (1994).
62. Grimme, S., Antony, J., Ehrlich, S. & Krieg, H. A consistent and accurate ab initio parametrization of density functional dispersion correction (DFT-D) for the 94 elements H–Pu. *J. Chem. Phys.* **132**, 154104 (2010).
63. Grimme, S. Semiempirical GGA-type density functional constructed with a long-range dispersion correction. *J. Comput. Chem.* **27**, 1787–1799 (2006).

Acknowledgements

The authors acknowledge Diamond Light Source for provision of beamtime at I20-EDE (SP21593-1). The Research Complex at Harwell is acknowledged for the use of facilities and staff support. The authors

acknowledge HarwellXPS for access to the national XPS facilities. UK Catalysis Hub is kindly thanked for resources and support provided via our membership of the UK Catalysis Hub Consortium and funded by EPSRC grants EP/R026939/1 (awarded to C.R.A.C.), EP/R026815/1 (awarded to C.R.A.C., P.P.W. and E.K.G.), EP/R026645/1 (awarded to C.R.A.C.), EP/R027129/1 and EP/M013219/1 (biocatalysis). P.P.W., E.K.G., K.M. and A.G. acknowledge EPSRC for funding (EP/V000691/1, awarded to P.P.W., E.K.G. and A.G.).

Author contributions

D.D., K.M., M.P., S.X. and L.L.K. performed the combined XAFS/DRIFTS study at Diamond Light Source. T.W., K.K. and H.K. contributed to the discussion around the potential role of rhodium carbide and prepared the rhodium carbide reference standard used for our linear combination XAFS analysis. M.Q. and C.R.A.C. performed and led on the computational aspects of the work. M.I. provided the XPS acquisition and data analysis. A.H.C. performed the MCR analysis. D.D. performed other catalytic testing and characterization work included in the manuscript. P.P.W., E.K.G. and A.G. conceived the experiments and supervised D.D. D.D. and P.P.W. wrote the manuscript and provided responses to the reviewer comments.

Competing interests

The authors declare no competing interests.

Additional information

Supplementary information The online version contains supplementary material available at https://doi.org/10.1038/s41929-024-01181-w.

Correspondence and requests for materials should be addressed to Alexandre Goguet or Peter P. Wells.

Peer review information *Nature Catalysis* thanks Santiago Figueroa, Arturo Martínez Arias and the other, anonymous, reviewer(s) for their contribution to the peer review of this work.